Creation of highly charged gold ion beam through collisional ionizations in a dense gold plasma driven by a femtosecond petawatt laser

Masayasu Hata ,[1,*] Chang Liu ,[1] James Kevin Koga ,[1] Natsumi Iwata ,[2] Yasuhiko Sentoku ,[2] and Mamiko Nishiuchi [1,†]
[1]*Kansai Institute for Photon Science, National Institutes for Quantum Science and Technology (QST), Kizugawa, Kyoto 619-0215, Japan*
[2]*Institute of Laser Engineering, The University of Osaka, Suita, Osaka 565-0871, Japan*

(Received 17 June 2025; accepted 1 August 2025; published 29 August 2025)

Numerical investigations of the ionization mechanisms in the high-temperature high-density gold plasma formed by a high-contrast high-intensity laser pulse interacting with gold foil are performed to investigate high-efficiency gold ion acceleration with few petawatt (PW)-level laser systems, aiming at producing $\gtrsim$10 MeV/u gold beams required to serve as an alternative to the front end of a conventional heavy-ion accelerator complex such as an ion source, linac, and drift tube linac. Short-pulse high-intensity laser pulses with a peak intensity of a few times 10^{22} Wcm^{-2}, which is not strong enough to expel Au L-shell electrons by laser field ionization, are shown to sufficiently resistively heat up the target bulk temperature so that collisional ionization by electrons in the plasma can expel L-shell electrons. The resultant highly charged Au ions ($\sim +72 \pm 4$) are exposed to the sheath field and accelerated to higher energies of $\sim$20 MeV/u.

DOI: 10.1103/8k98-6q48

I. INTRODUCTION

The laser-driven heavy-ion acceleration scheme is attractive for many fields of potential applications, such as heavy-ion accelerators [1,2], fission-fusion reactions [3], fusion research [4], and the generation of the warm dense matter [5]. Recent drastic improvements in laser technology have enabled the increase in the laser peak intensity to more than 10^{23} Wcm^{-2} [6]. This has brought about the capability of acceleration of not only high-energy light ions but also heavier ones by the laser-driven ion acceleration scheme [7,8].

If heavy ions are highly charged in the early stage of the acceleration and exposed to the strong acceleration field, they can be efficiently accelerated. However, it is difficult to achieve this condition even if special care is taken with the target [7,8] because the ionization potential of the inner shell electrons of heavy ions is very high, i.e., $\sim$8 keV for M shell, $\sim$20 keV for L shell, and $\sim$100 keV for K shell, for gold atoms. Even a laser pulse from a petawatt (PW)-class laser system with an intensity of 10^{21} (10^{22}) Wcm^{-2} cannot expel all the electrons in the M shell (L shell) by laser field ionization process alone.

However, considering the fact that the ionization potential density (pressure) of solid gold is $P_{\mathrm{Au}} \sim 5$ petapascal (PPa) and the laser energy density of even a PW-class laser with an intensity of 10^{21} Wcm^{-2} exceeds 30 PPa, the laser pulse, in principle, can heat a solid Au to the energy density sufficiently higher than the ionization pressure and remove the electrons from a gold atom by other ionization processes, for example, electron/photon impact ionizations.

Investigations on the contributions of different ionization mechanisms to the accelerated heavy-ion beams have been carried out [7–10]. Nevertheless, the way to achieve high-efficiency acceleration of the heavy-ion beam is still not clear. Afshari *et al.* [10] pointed out that electron impact ionization contributes significantly to make highly charged gold ions whose charge states have $Z > 70$ in the plasma by a picosecond laser pulse with a peak intensity of several times 10^{20} Wcm^{-2} interacting with a gold target; however, the charge states of the accelerated gold ions to high energies are relatively lower, such as $\sim$50. These highly charged gold ions are only accelerated up to a few MeV/u [8].

This is because a longer time is necessary for the gold ions in the plasma with relatively low density to be highly charged than the lifetime of the strong sheath field. To make the highly charged plasma within the lifetime of the sheath field, a high-contrast short-pulse laser is suitable [9], because it can potentially input the laser energy and heat up the target before it expands, maintaining both a high sheath field strength and high collisional ionization rate.

In this paper, we numerically investigate the ionization mechanisms in a high-temperature high-density gold plasma formed by a high-contrast high-intensity laser pulse interacting with a 200-nm gold target. Aiming to produce a gold ion beam over 10 MeV/u energies, which is required for serving as an alternative to the front end of a conventional accelerator system such as an ion source, linac, and drift tube linac, high-efficiency gold ion acceleration schemes are investigated with a few PW-level femtosecond laser system. We demonstrate that short-pulse high-intensity laser pulses with a peak intensity of a few times 10^{22} Wcm^{-2}, which is not

*Contact author: hata.masayasu@qst.go.jp
†Contact author: nishiuchi.mamiko@qst.go.jp

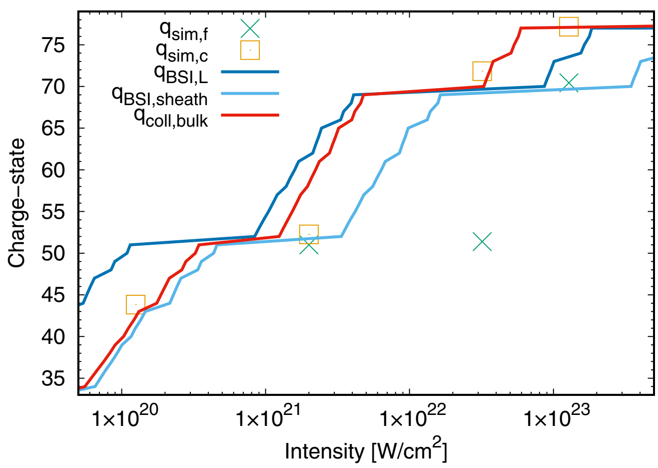

FIG. 1. Average charge state behavior of accelerated gold ions against the laser intensity. The blue and sky blue lines indicate the charge states achieved by the ionizations of laser field and rear sheath field using BSI model, respectively. The red line indicates the charge states achieved by the collisional ionization assuming resistively heated thermal electrons ionize the gold ions with an ionization potential equal to the thermal electron energy. The green cross and orange square show the results from particle-in-cell (PIC) simulations ($q_{\rm sim,f}$, $q_{\rm sim,c}$) explained later in the text. The points show the average charge state of ions whose energies exceed 80% of the maximum energy.

strong enough to expel L-shell electrons around the Au ions by laser field ionization, can effectively heat up the target bulk temperature high enough such that the collisional ionization process can expel the L-shell electrons if we can maintain a sufficiently high target density. The resultant highly charged Au ions ($\sim +72 \pm 4$) are exposed to the sheath field and accelerated to higher energies of ~20 MeV/u.

II. IONIZATION MECHANISMS AND ACHIEVABLE CHARGE STATES

Which ionization mechanism dominates in the gold plasma produced by short-pulse few-PW class laser system strongly depends on the intensity of the incident laser pulse. Figure 1 shows the prediction for the achievable ionization states of the gold ions with the function of the laser intensity by the simple models explained below. Here, we assume the 45-fs laser pulses within intensity range of 1.0×10^{20} to 1.0×10^{23} Wcm^{-2} are irradiated on 200-nm-thick gold targets. The blue and sky blue lines indicate the charge states achievable by the ionizations of laser field amplitude $E_L = \sqrt{2I_L/\epsilon_0 c}$ with the laser intensity I_L, the permittivity of vacuum ϵ_0, and the speed of light c and rear sheath field using barrier suppression ionization (BSI) model [11], where the electric field $E_{\rm BSI}$ required to ionize an ion with charge state $Z-1$ and ionization potential in electron volts (eV) $I_{P[\rm eV]}$ to charge state Z is obtained by the following equation: $E_{BSI} = 1.7 \times 10^8 I_{P[\rm eV]}^2/Z$ [V/m]. The rear sheath field strength E_s under 1D geometry condition is evaluated by the formula $E_s = E_L\sqrt{\eta_1/2}$ [9], where the conversion efficiency from the laser to hot electrons η_1 is assumed to be 0.5.

On the other hand, the collisional ionization process is ongoing in the hot gold plasma heated by the resistive heating process. Under the conditions of 1D geometry and sufficient relativistic laser intensity $a_0 \gg 1$, the resistively heated up bulk electron temperature of the target satisfies the relation

$$\bar{T}_e \sim \left(\frac{5}{3}\frac{\eta_0 \ln\Lambda \gamma^2 \bar{t}}{\bar{n}_i}\right)^{2/5}, \qquad (1)$$

where $\ln\Lambda$ is the Coulomb logarithm, $\bar{n}_i$ is the bulk ion density normalized by the critical density n_{cr}, $\bar{T}_e$ is the bulk electron temperature normalized by $m_e c^2$, $\bar{t}$ is the heating time normalized by the laser oscillation period, γ is the relativistic factor of hot electrons, $\eta_0 = e^2\omega_0/(4\pi\epsilon_0 m_e c^3)$ is a constant, and we here estimate based on the ponderomotive scaling [12] as $\gamma = (1 + \eta_1 a_0^2/2)^{1/2}$. The red line in Fig. 1 indicates the charge states achieved by the collisional ionization in this way, assuming resistively heated thermal electrons ionize the gold ions with an ionization potential equal to the thermal electron energy, namely, $I_P \sim \bar{T}_e$. Here, we assume $\ln\Lambda \sim 5$, $\eta_1 = 0.5$, $\bar{n}_i = 34$ as the solid gold ion density, and $\bar{t} = 17$ as the typical pulse duration of J-KAREN-P laser (i.e., 45 fs for 800 nm wavelength). When the laser intensity is sufficiently high ($a_0 \gg 1$), the relation $\gamma \propto \eta_1 I/2$ provides a good approximation. Under this condition, if either the Coulomb logarithm $\ln\Lambda$ or η_1 doubles, the required laser intensity is halved. Conversely, if either is halved, the required laser intensity doubles. In the simulations presented later, the laser absorption rate, which corresponds to the laser coupling efficiency to electrons, ranges from 39% to 59%. The Coulomb logarithm, which depends on the plasma state, typically varies within the range 5–10. Therefore, although the required laser intensity may shift by a factor of two depending on these parameters, it does not exhibit drastic changes.

As can be seen in Fig. 1, the ionization potential is proportional to the power of 1/2 of the electric field in the BSI model and to the power of 4/5 of the laser electric field in the relativistic limit ($a_0 \gg 1$) for collisional ionization, so that even ions with higher ionization potentials can be ionized by collisional ionization when the laser intensity is increased. Therefore, for ions with large atomic numbers and large ionization potentials, collisional ionization at high laser intensities can be used to achieve high degree of ionization. In the case of solid gold targets, collisional ionization by resistively heated bulk electrons becomes dominant over ionization by the laser field at intensities above 10^{22} Wcm^{-2}.

Conversely, ions with small atomic numbers have such low ionization potentials that they can be completely ionized by electric field ionization at relatively low laser intensities. The BSI model shows that carbon, for example, is fully ionized at $\sim 6 \times 10^{18}$ Wcm^{-2}. In this low-intensity regime, collisional ionization due to resistively heated bulk electrons occurs inefficiently. However, collisional ionization by fast electrons may still play a significant role, owing to their relatively low energies at such intensities. These effects should be taken into account when modeling ionization dynamics under low-intensity laser conditions.

In the case of gold ions, the laser field ionization process might bring us the highest gold charge state in the plasma at laser intensities below a few times 10^{21} Wcm^{-2}. However, the laser field ionization is usually dominant in the preplasma in front of the target and the highly charged ions by the laser field ionization are not exposed to the sheath field at the rear side of the target if the target is kept opaque. This condition is confirmed by the particle-in-cell (PIC) simulations, which will be described later in the paper. Therefore, the collisional ionization process dominates over any other ionization processes in the gold ion plasma until the laser intensity is high enough such that the target density is comparable to the relativistic critical density of the laser (in our case, the laser intensity of more than a few times 10^{23} Wcm^{-2}, which will be also confirmed by the PIC simulation later in this paper). If we can make good use of the collisional ionization process, we might be able to achieve highly efficient gold ion acceleration. To achieve this, we need to setup the strong acceleration field at the right timing and right place, which we will examine by the PIC simulations in the following sections.

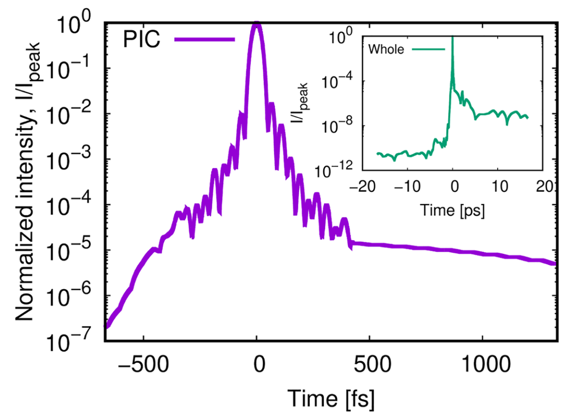

FIG. 2. The temporal profile of the normalized laser intensity in the simulations. The inset shows the whole temporal profile measured in the experiment. A portion of the experimentally obtained profile is selected out and used in the PIC simulation.

III. SIMULATION SETUP

We use the PICLS-2D code that includes binary collisions among charged particles, dynamic ionization processes in gas and solid density plasmas, and radiation processes [13–16]. In the code, a binary collision model is implemented to appropriately account for interactions between charged particles of different weights and has been extended to the relativistic regime [14]. The model is further enhanced to incorporate the effects of bound electrons, enabling accurate treatment of collisions in partially ionized plasmas [13]. The ionization model incorporates both field ionization and collisional ionization, calculating time-dependent ionization probabilities and determining ionization events using random numbers. For field ionization, the method follows the approach proposed by Kato *et al.* [17], while collisional ionization is treated using the Lotz formula [18]. Ionization potentials are taken from NIST data [19], and potential lowering effects are accounted for using the Ecker-Kröll model [20]. PICLS calculates radiation losses due to free-free and bound-bound emissions [13]. The free-free, bound-bound, and bound-free emissivity for solid gold are precomputed by using the FLYCHK code [21] with the same methods as in Ref. [13] and incorporated into the model. Compared to detailed atomic codes, the FLYCHK code is simpler and more robust, though its accuracy is relatively limited. In this study, FLYCHK results were used as a zeroth-order approximation. For more precise calculations, it is necessary to employ detailed atomic codes such as the Flexible Atomic Code [22] or HULLAC [23]. In the current calculation, the electron temperature range is extended up to 11 keV. It is also confirmed that the bound-free is always more than an order of magnitude lower than free-free and bound-bound; thus we ignored it in the radiation model. The radiation transport is not incorporated for the current simulation because the target thickness is thinner than the attenuation length of ∼keV X-rays. Additionally, the radiative damping effects are not negligible for the high intensity of more than 10^{22} Wcm^{-2}, as pointed out in Ref. [24]. Radiative damping, also known as radiation reaction, refers to the effect in which a charged particle experiences a recoil force due to its own emitted radiation. This effect becomes significant when the particle undergoes strong acceleration. Although the effects depend on various conditions, we considered the radiation damping effects. Among the several models available for describing radiation damping, this study adopts an approach based on the Lorentz-Abraham-Dirac (LAD) equation, incorporating terms up to the second order into the simulation [15].

A relatively thick gold target ($Z = 79$) is irradiated by the short-pulse high-contrast laser pulses to investigate how the transition of the dominating ionization mechanisms is as a function of laser intensity. We use the plasma mirror (PM) cleaned temporal profile of the J-KAREN-P laser system [25]. Figure 2 shows the measured temporal profile of the J-KAREN-P laser system, which is used in the simulations. The inset shows the measured whole temporal profile. The laser pulse has a contrast level of 10^{10} 2 ps before the main pulse peak. The peak intensity of the laser is varied from 1.3×10^{20}, 2.0×10^{21}, 3.2×10^{22}, and 1.3×10^{23} Wcm^{-2} (the corresponding a_0 are 7.8, 31, 122, and 252 where a_0 is the normalized laser intensity described as $(eE_L)/(m_e\omega_L c)$ or $[e\sqrt{2I/(\epsilon_0 c)}]/(m_e\omega_L c)$) assuming that the laser temporal contrast curve is kept the same. The central wavelength and spot diameter are set to 800 nm and 1.5 μm (FWHM), respectively. The target consists of a prepulse-made gold preplasma, gold bulk plasma, and contaminants. Assuming fairly small preplasma made by PM cleaned high-contrast laser, the preplasma has an exponential ion density profile in the target normal direction with a scale length of 28 nm from the density of 0.003 to $30n_{\mathrm{cr}}$, where $n_{\mathrm{cr}} = (\omega_0^2 m_e)/(4\pi e^2)$ means the critical density of the laser with the laser frequency ω_0, electron mass m_e, and elementary charge e. The gold bulk plasma has a flat density profile with a solid density of $34n_{\mathrm{cr}}$ and a thickness of 200 nm. The contaminants are made of hydrogen and carbon and have a flat profile with a density of $3.3n_{\mathrm{cr}}$ and a thickness of 10 nm, representing a contaminant with 1 nm thickness at solid density ($= 33n_{\mathrm{cr}}$) where the line density is retained by reducing the density and increasing the thickness. The number of the ions per cell is set to 10 for all species. The atomic numbers of gold, carbon, and hydrogen are 79, 6, and 1, respectively. The initial charge state of the target is set to 1 for hydrogen and 2 for all the other ion species. The sizes of the cell and time step are set to 10 nm and

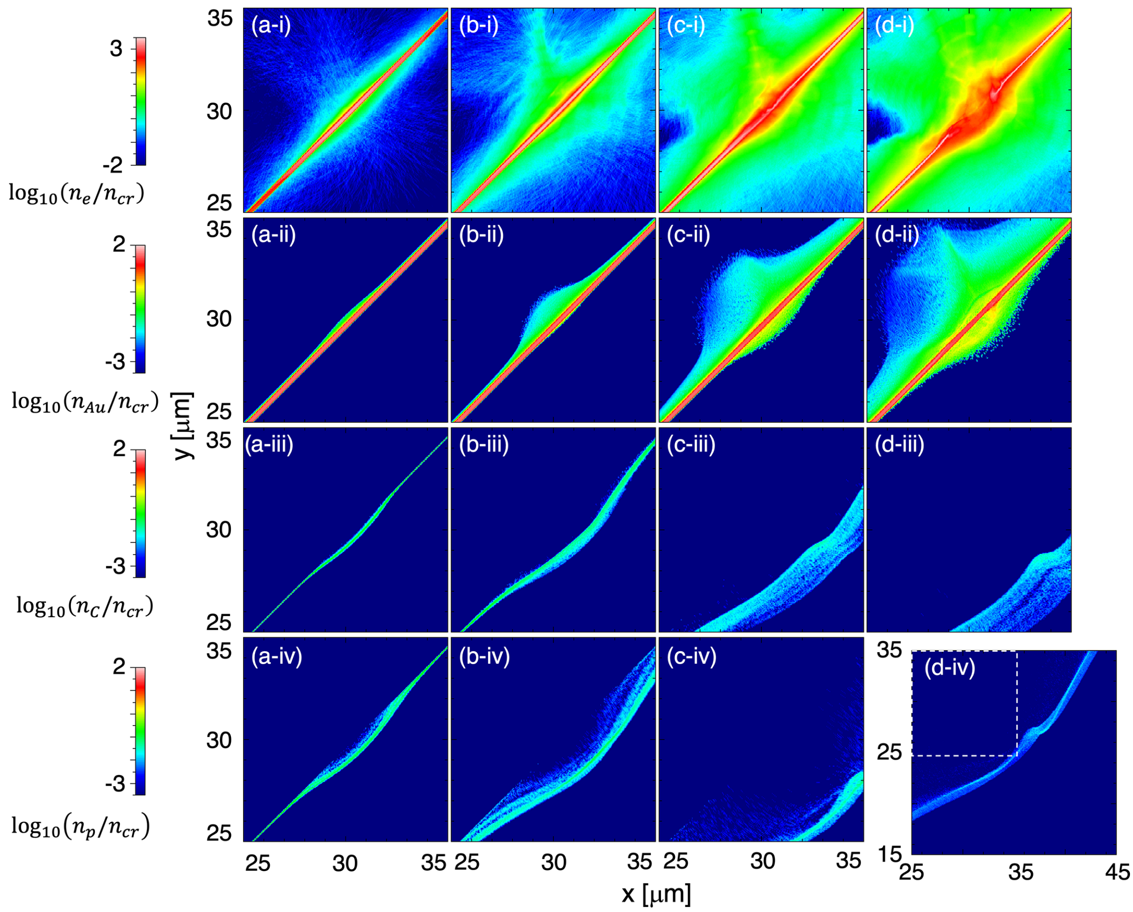

FIG. 3. The spatial density profiles of (i) electrons, (ii) gold ions, (iii) carbon ions, and (iv) protons at the laser peak irradiation timing ($t = 0$ fs) in the case of the intensities of (a) 1.3×10^{20}, (b) 2.0×10^{21}, (c) 3.2×10^{22}, and (d) 1.3×10^{23} Wcm^{-2}. The laser propagates along the x-axis from the left boundary. Only panel (d-iv) is a zoomed-out view to trace the accelerated protons; the dashed region is the same box size as in the other figures.

33.4 as, respectively. The simulation box size is $(L_x, L_y) =$ (65 μm, 60 μm). The target is tilted at a 45° angle. A linearly P-polarized laser beam is injected from the boundary in the negative x direction, and it is focused onto the surface of the bulk plasma at an oblique incidence angle of 45°. We adopt the absorbing boundary condition for the electromagnetic fields and the reflection boundary condition for particles except for fast electrons with a Lorentz factor of more than 2, since they move out from the interaction region and rarely return during the simulation time. Under these conditions, we performed the simulation from 0.77 ps before the main pulse peak arrives at the target surface until 1.23 ps after that timing.

IV. RESULTS AND DISCUSSION

Figure 3 shows spatial density profiles of (i) electrons, (ii) gold ions, (iii) carbon ions, and (iv) protons at the laser peak irradiation timing ($t = 0$ fs) for each laser intensity. The laser propagates along the x-axis from the left boundary and focuses the target surface at $(x, y) =$ (30 μm, 30 μm) with an incidence angle of 45°. The target maintains a high electron density above $1000n_{\rm cr}$ at the timing of main pulse irradiation with intensities below 3.2×10^{22} Wcm^{-2}, as shown in Figs. 3(a-i), 3(b-i), and 3(c-i) because the relativistic critical densities for the intensities of 1.3×10^{20}, 2.0×10^{21}, and 3.2×10^{22} Wcm^{-2} are 7.7, 31, and $122n_{\rm cr}$, respectively. The transmitted laser energies after the interaction for the cases of intensities below 3.2×10^{22} Wcm^{-2} are less than 1.02% of the intrinsic laser energy. In contrast, the electron density at the focus decreases $\sim 250n_{\rm cr}$ at the peak of the pulse for the highest intensity case of 1.3×10^{23} Wcm^{-2}, where the electron density is getting close to the relativistic critical density $244n_{\rm cr}$. Therefore, the relativistically induced transparency is triggered and the laser penetrates through the target; thus the transmitted laser energy reaches 35.6%.

Ions with a higher charge-to-mass ratio are accelerated faster by the electric field and travel farther in a shorter time. Such features, i.e., that the protons are accelerated more efficiently than carbons, are shown in the whole intensity range of our simulations. Especially, in the highest intensity case, the protons fly away from the target surface, expanding in much larger area than that of the other cases at the timing of laser peak [Fig. 3(d-iv)]. In general, ions originating from the contaminant layer shield the acceleration electric field and prevent the ions from the bulk of the target from being efficiently accelerated. The shielding becomes effective in the case of lower intensity of the laser because the ions from

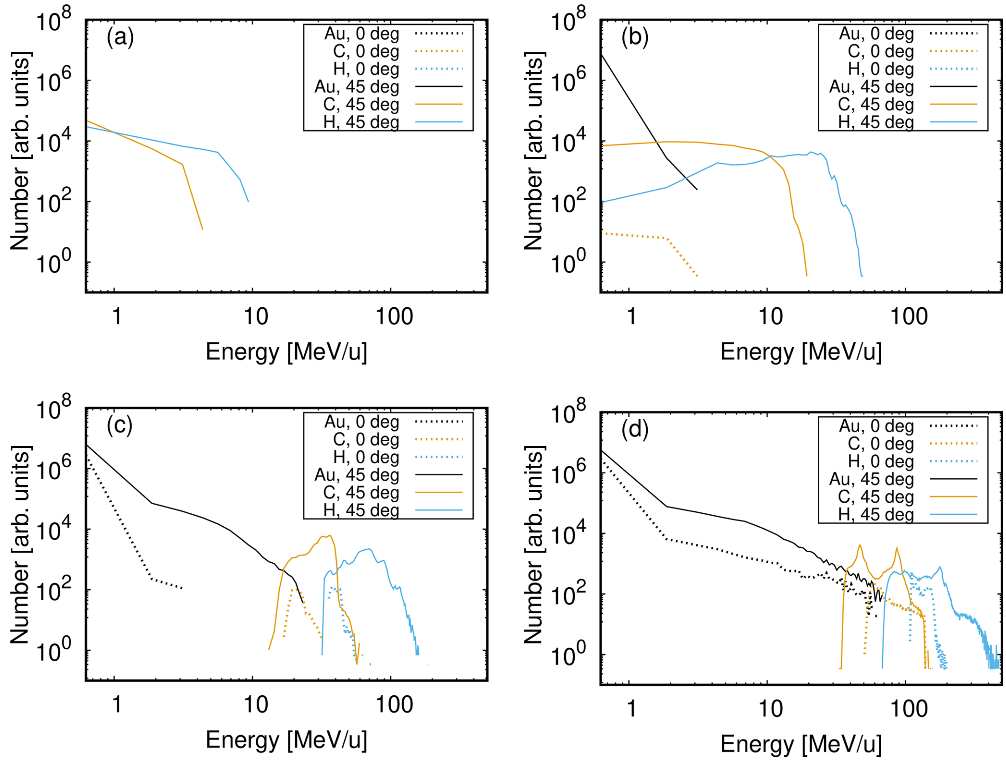

FIG. 4. Ion energy spectra 170 fs after the laser peak irradiation in the case of the intensities of (a) 1.3×10^{20}, (b) 2.0×10^{21}, (c) 3.2×10^{22}, and (d) 1.3×10^{23} $\mathrm{Wcm^{-2}}$, where 0° and 45° indicate the directions of the laser propagation and target normal, and only ions within plus or minus 22.5° from each direction are measured. The time after 170 fs is just before the fastest proton reaches the boundary of the simulation box for the intensity of (d) 1.3×10^{23} $\mathrm{Wcm^{-2}}$.

contaminant layer are still near around the target during the lifetime of the acceleration field. In the lowest intensity case, only the ions from the contaminant layer are accelerated at the laser peak, and the gold ions hardly move from its initial position [Fig. 3(a-ii)].

Figure 4 shows ion energy spectra in the case of the intensities of (a) 1.3×10^{20}, (b) 2.0×10^{21}, (c) 3.2×10^{22}, and (d) 1.3×10^{23} $\mathrm{Wcm^{-2}}$ at $t = +170$ fs, where 0° and 45° indicate the directions of the laser propagation and target normal, and only ions within plus or minus 22.5° from each direction are measured. Here, $t = +170$ fs is just before the fastest proton reaches the boundary of the simulation box for the highest intensity of 1.3×10^{23} $\mathrm{Wcm^{-2}}$ [Fig. 4(d)]. Only contaminant ions are accelerated at the intensity of 1.3×10^{20} $\mathrm{Wcm^{-2}}$ as shown in Fig. 4(a), which is also confirmed in Fig. 3(a-ii). This is mainly because the gold ions are not highly ionized and are not exposed to the sheath field, while the strength of the acceleration field is still high. The maximum accelerated gold ions in the lowest intensity case have an energy of only 0.24 MeV/u (0.023c) even at the final time of the simulation. Gold ions are accelerated > MeV/u energy range with the laser intensities above 2.0×10^{21} $\mathrm{Wcm^{-2}}$. The whole contaminant layer is detached far away from the target before the arrival of the main pulse to the target surface; thus only gold ions from the bulk of the target are accelerated by the strong sheath field established by the main pulse for the cases of laser intensities of 3.2×10^{22} and 1.3×10^{23} $\mathrm{Wcm^{-2}}$, which was also clearly demonstrated in our previous experimental investigations with relatively lower laser intensity irradiated on a silver target [9].

Ions are mostly accelerated toward target normal direction in all intensity ranges of the current simulations. The component of accelerated ions in the laser propagation direction increases at the intensity of 1.3×10^{23} $\mathrm{Wcm^{-2}}$, but still the target normal component is dominating. Note that the spectral peaks seen for the intensity of 1.3×10^{23} $\mathrm{Wcm^{-2}}$ [Fig. 4(d)] are caused by the spatially nonuniform acceleration field feature, which is a result of the target density deformation by the rising edge of the laser itself. Even though the ions show peaks in the spectra, they are accelerated in a variety of directions such that they might not be suitable for applications.

Figure 5 shows the energy spectra and average charge state of gold ions and their proportion of final ionization processes recorded at 340 fs after the laser peak irradiation for the intensities of (a) 2.0×10^{21}, (b) 3.2×10^{22}, and (c) 1.3×10^{23} $\mathrm{Wcm^{-2}}$, where the black line indicates energy spectra, and dark violet and green lines indicate average charge state of gold ions finally ionized by field and collision, respectively.Violet and light green colors in the bar graphs indicate the ratio of field and collisional ionization events, respectively. The time after 340 fs is just before the fastest gold ion reaches the boundary of the simulation box for the intensity of 1.3×10^{23} $\mathrm{Wcm^{-2}}$ [Fig. 5(c)]. Here, only gold ions with a traveling direction of −45° to 135° are measured, with respect to the laser propagation direction as 0° and rear surface normal oriented at 45° (see Fig. 3, where 0° corresponds to the positive x-direction and 45° corresponds to the direction pointing diagonally downward to the right). The figure for the intensity of 1.3×10^{20} $\mathrm{Wcm^{-2}}$ is not shown because

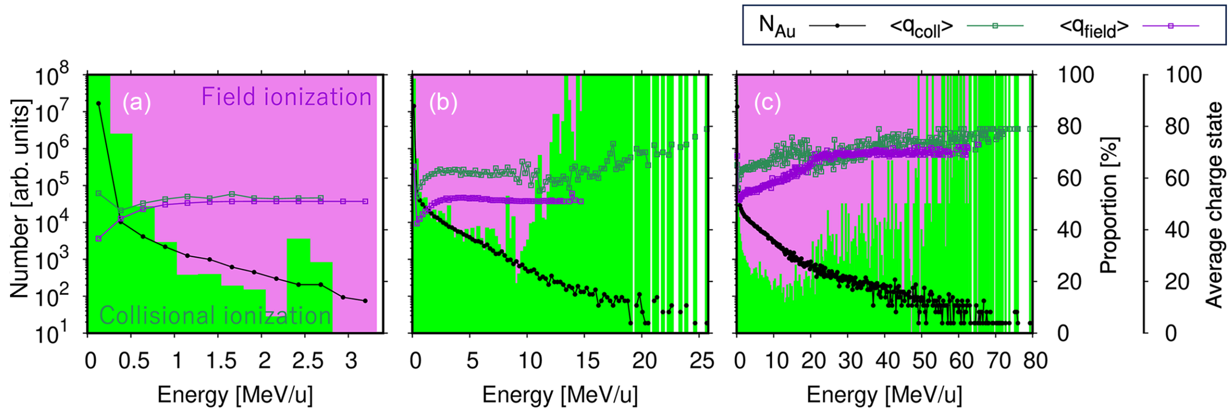

FIG. 5. The energy spectra and average charge state of gold ions and their proportion of final ionization processes 340 fs after the laser peak irradiation for the intensities of (a) 2.0×10^{21}, (b) 3.2×10^{22}, and (c) 1.3×10^{23} $\mathrm{Wcm^{-2}}$, where the black line (N_{Au}) indicates energy spectra, dark violet ($\langle q_{\mathrm{field}} \rangle$) and green ($\langle q_{\mathrm{coll}} \rangle$) lines indicate average charge state of gold ions finally ionized by field and collision, respectively, and violet and light green colors in the bar graphs indicate proportions of field ionization and collisional ionization, respectively. The time after 340 fs is just before the fastest gold ion reaches the boundary of the simulation box for the intensity of (c) 1.3×10^{23} $\mathrm{Wcm^{-2}}$. Here, only gold ions with a traveling direction of $-45°$ to $135°$ are measured when the laser and rear surface normal directions are 0° and 45°, respectively. The figure for the intensity of 1.3×10^{20} $\mathrm{Wcm^{-2}}$ is not shown because no gold acceleration occurred, as shown in Fig. 2(a).

efficient gold acceleration does not happen [Fig. 3(a)]. The bulk temperature was low to ionize the bulk gold ions efficiently [Fig. 6(a)].

At the intensity of 2.0×10^{21} $\mathrm{Wcm^{-2}}$ [Fig. 4(a)], the final ionization process for high-energy accelerated gold ions is dominated by field ionization in the sheath field at the target rear side, while the ratio of collisional ionization increases as the energies of the accelerated gold ions lower. Our previous study has shown that highly charged ions are accelerated by the sheath field when the resistively heated area of the hot plasma, in which atoms are collisionally ionized to high-charge states, reached the target rear surface within the duration of the sheath field lifetime [9]; see Figs. 5(b) and 5(c) for this case. At low intensities, a large number of highly ionized gold ions are produced in the target bulk by collisions [Figs. 6(e) and 6(f)]. These ions are extracted by the sheath field after the field weakens, thus not accelerated to high energies. The average charge states are +51 for collisional and sheath field ionization processes (also shown in Fig. 1, green cross and orange square). According to the BSI model [11], the required sheath fields to ionize gold ions with the charge states of +51 and +52 are 29 and 79 TV/m, respectively. The observed peak sheath field is 78.1 TV/m, which explains the low average ionization states around +51, resulting in the limited energy about a few MeV/u of gold ions.

At the laser intensity of 3.2×10^{22} $\mathrm{Wcm^{-2}}$, the recorded final ionization process for high-energy accelerated gold ions is dominated by collisional ionization, and contributions of collisional and field ionization processes are comparable for low-energy accelerated gold ions. The average charge state

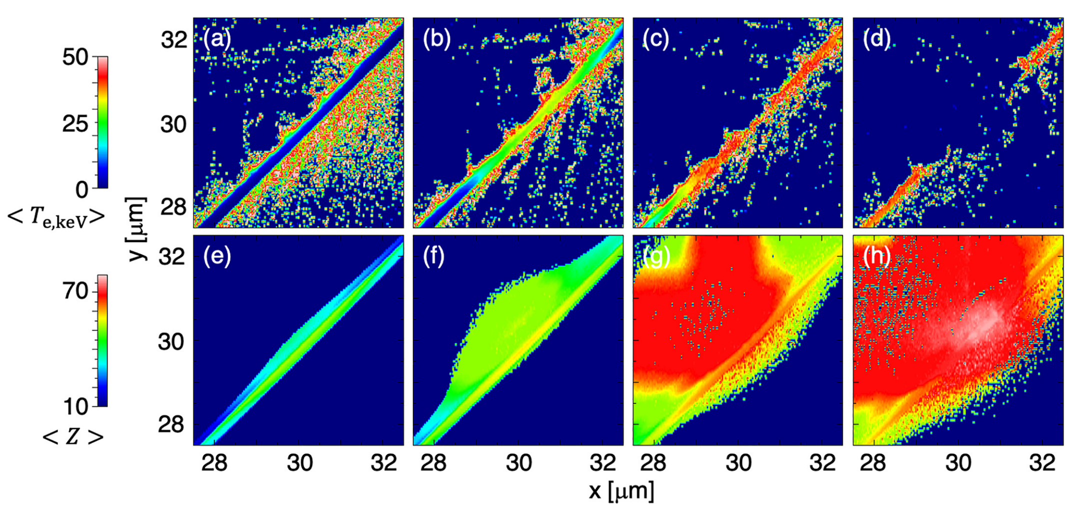

FIG. 6. Spatial profiles of (a)–(d) the bulk electron temperature and (e)–(h) average gold ion charge state at the laser peak irradiation timing (t = 0 fs) for the intensities of (a) and (e) 1.3×10^{20}, (b) and (f) 2.0×10^{21}, (c) and (g) 3.2×10^{22}, and (d) and (h) 1.3×10^{23} $\mathrm{Wcm^{-2}}$. Here, the bulk temperature is obtained by averaging electrons with energies below 100 keV. Regions with no electrons or where all electrons exceed 100 keV are set to zero temperature.

of the finally field-ionized gold ions accelerated to higher energy (up to ∼15 MeV/u) stays at +51. Actually, there are some gold ions ionized by the sheath field to +65 (i.e., the peak sheath field is 147 TV/m) but they are further ionized by the collisions to even higher charge states. The target bulk temperature is heated up to 45 keV at the time of main pulse interaction [Fig. 6(c)] and collisional ionization in the high-temperature plasma produced many high-charge-state gold ions. The average charge state of the collisionally ionized ions is around +60 with the energies of 3–15 MeV/u and up to 79 with higher energies. The achieved charged state by collisional ionization (+79 at maximum and $+72 \pm 3$ when taking the average of ions with energies within 20% of the highest energy) is well above that achieved by the field ionization ($\sim + 51$). Both field-ionized and collisionally ionized ions are accelerated by the sheath field depending on their charge to mass ratio; thus the collisionally ionized ions gain higher energies. The results are consistent with the simple analytical estimate that the collisional ionization in a plasma heated up to high temperature can have an important role for the highly charged gold acceleration shown in Sec. II (Fig. 1).

At the high intensity of 1.3×10^{23} Wcm^{-2}, the final ionization process for high-energy accelerated gold ions is dominated by collisional ionization, and collisional and field ionization processes have a comparable effect for the accelerated gold ions to moderate-energy range. A bit later than the timing of main pulse peak, the target becomes relativistically transparent and the laser pulse can penetrate deep inside the target. As a result, gold ions are ionized by the laser field to +73, and higher charge states up to +79, i.e., full ionization, are generated by collisions in the resistively heated target bulk [Fig. 6(h)]. The average ionization degree due to collisional ionization is higher, reaching full ionization. Even though the relativistic transparency is triggered, the main acceleration mechanism for the gold ions is observed to be Target Normal Sheath Acceleration (TNSA). Because of achieved high-charge states, the maximum energy of the accelerated gold ions is ∼70 MeV/u.

At high laser intensity, radiative losses due to free-free and bound-bound transitions might affect the acceleration performance. However, even at the highest laser intensities, the radiation losses were less than 0.001% of the injected laser energy, and its effect on the bulk electron temperature, and thus on the collisional ionization rate, was negligibly small. The radiative losses via radiative damping were larger than those of the free-free and bound-bound emissions, but only 0.11% and 0.85% at 3.2×10^{22} and 1.3×10^{23} Wcm^{-2} laser intensities, respectively; thus the effect of the radiative damping was not so large in the present simulations.

V. SUMMARY

The laser intensity dependence of the final ionization mechanism of accelerated ions in the TNSA scheme with a 200-nm gold target is investigated. The final ionization mechanism for energetic ions is dominated by collisional ionization as the laser intensity increases. At the lower laser intensity of 1.3×10^{20} Wcm^{-2}, the acceleration of gold is completely suppressed, as the contaminants cannot be entirely removed within the duration of the sheath field, thereby shielding the sheath electric field from the bulk gold. At the relatively low laser intensity of 2.0×10^{21} Wcm^{-2}, the sheath field is capable of almost completely expelling the contaminant layer, allowing for the acceleration of the bulk gold. However, due to insufficient resistive heating and collisional ionization within the duration of the sheath field, the acceleration of gold to high-charge states and high energies is predominantly driven by field ionization induced by the sheath electric field. When the laser intensity is high, the heating proceeds sufficiently at the rear surface within the lifetime of the acceleration field and highly charged ions are extracted and accelerated. However, at the highest laser intensity, the laser becomes relativistically transparent around the peak of the pulse and the contribution of the laser field ionization increases; nevertheless, collisional ionization is still dominating.

We have demonstrated that short-pulse high-intensity laser pulses with a peak intensity of few times 10^{22} Wcm^{-2} can resistively heat up the target bulk temperature high enough such that the collisional ionization process can expel L-shell electrons with an ionization potential of ∼20 keV levels, if we can keep the target density sufficiently high. The resultant highly charged Au ions ($\sim + 72 \pm 4$) are exposed to the sheath field and accelerated to higher energies of ∼20 MeV/u, which satisfies the requirement of the injector for a heavy-ion accelerator complex.

The understanding of the detail ionization mechanisms obtained in the current paper paves the way for controlling the production of highly charged high-energy heavy-ion beams by short-pulse high-intensity laser systems. This knowledge is useful for the realization of a next-generation injector for compact heavy-ion accelerators.

ACKNOWLEDGMENTS

This work was supported by JST-Mirai Program Grant No. JPMJMI17A1, Japan. This work was supported by JSPS KAKENHI Grants No. JP24H00204, No. JP23K03354, No. JP23K20038, No. JP22H00121, No. JP21KK0049, and No. JP20H00140. This work was supported by the Institute of Laser Engineering, the University of Osaka through Joint Research Projects No. 2025B2-033HATA, No. 2024B2-036HATA, No. 2023B2-035HATA, No. 2022B2-040HATA, No. 2025B2-055NISHIUCHI, No. 2024B2-017NISHIUCHI, and No. 2023B2-041NISHIUCHI. This research was conducted with the supercomputer HPE SGI8600 in the National Institutes for Quantum Science and Technology (QST). This work was partly achieved using SQUID at the D3 Center, the University of Osaka.

DATA AVAILABILITY

The data that support the findings of this article are not publicly available upon publication because it is not technically feasible and/or the cost of preparing, depositing, and hosting the data would be prohibitive within the terms of this research project. The data are available from the authors upon reasonable request.

[1] S. Busold, D. Schumacher, C. Brabetz, D. Jahn, F. Kroll, O. Deppert, U. Schramm, T. E. Cowan, A. Blažević, V. Bagnoud, and M. Roth, Towards highest peak intensities for ultra-short MeV-range ion bunches, Sci. Rep. **5**, 12459 (2015).

[2] P. N. Ostroumov and K. W. Shepard, Multiple-charge beam dynamics in an ion linac, Phys. Rev. Spec. Top. Accel. Beams **3**, 030101 (2000).

[3] D. Habs, P. G. Thirolf, M. Gross, K. Allinger, J. Bin, A. Henig, D. Kiefer, W. Ma, and J. Schreiber, Introducing the fission–fusion reaction process: using a laser-accelerated Th beam to produce neutron-rich nuclei towards the $N = 126$ waiting point of the *r*-process, Appl. Phys. B **103**, 471 (2011).

[4] S. Kawata, T. Karino, and A. I. Ogoyski, Review of heavy-ion inertial fusion physics, Matter Radiat. Extremes **1**, 89 (2016).

[5] W. Bang, B. J. Albright, P. A. Bradley, D. C. Gautier, S. Palaniyappan, E. L. Vold, M. A. S. Cordoba, C. E. Hamilton, and J. C. Fernández, Visualization of expanding warm dense gold and diamond heated rapidly by laser-generated ion beams, Sci. Rep. **5**, 14318 (2015).

[6] J. W. Yoon, Y. G. Kim, I. W. Choi, J. H. Sung, H. W. Lee, S. K. Lee, and C. H. Nam, Realization of laser intensity over 10^{23} W/cm^2, Optica **8**, 630 (2021).

[7] P. Wang, Z. Gong, S. G. Lee, Y. Shou, Y. Geng, C. Jeon, I. J. Kim, H. W. Lee, J. W. Yoon, J. H. Sung, S. K. Lee, D. Kong, J. Liu, Z. Mei, Z. Cao, Z. Pan, I. W. Choi, X. Yan, C. H. Nam, and W. Ma, Super-heavy ions acceleration driven by ultrashort laser pulses at ultrahigh intensity, Phys. Rev. X **11**, 021049 (2021).

[8] F. H. Lindner, E. McCary, X. Jiao, T. M. Ostermayr, R. Roycroft, G. Tiwari, B. M. Hegelich, J. Schreiber, and P. G. Thirolf, En-route to the fission–fusion reaction mechanism: a status update on laser-driven heavy ion acceleration, Plasma Phys. Controlled Fusion **61**, 055002 (2019).

[9] M. Nishiuchi, N. P. Dover, M. Hata, H. Sakaki, K. Kondo, H. F. Lowe, T. Miyahara, H. Kiriyama, J. K. Koga, N. Iwata *et al.*, Dynamics of laser-driven heavy-ion acceleration clarified by ion charge states, Phys. Rev. Res. **2**, 033081 (2020).

[10] M. Afshari, S. Morris, L. D. Geulig, Z. M. Chitgar, P. Gibbon, P. G. Thirolf, and J. Schreiber, The role of collisional ionization in heavy ion acceleration by high intensity laser pulses, Sci. Rep. **12**, 18260 (2022).

[11] S. Augst, D. D. Meyerhofer, D. Strickland, and S. L. Chin, Laser ionization of noble gases by Coulomb-barrier suppression, J. Opt. Soc. Am. B **8**, 858 (1991).

[12] S. C. Wilks, W. L. Kruer, M. Tabak, and A. B. Langdon, Absorption of ultra-intense laser pulses, Phys. Rev. Lett. **69**, 1383 (1992).

[13] R. Mishra, P. Leblanc, Y. Sentoku, M. S. Wei, and F. N. Beg, Collisional particle-in-cell modeling for energy transport accompanied by atomic processes in dense plasmas, Phys. Plasmas **20**, 072704 (2013).

[14] Y. Sentoku and A. J. Kemp, Numerical methods for particle simulations at extreme densities and temperatures: Weighted particles, relativistic collisions and reduced currents, J. Comput. Phys. **227**, 6846 (2008).

[15] R. R. Pandit and Y. Sentoku, Higher order terms of radiative damping in extreme intense laser-matter interaction, Phys. Plasmas **19**, 073304 (2012).

[16] Y. Sentoku, I. Paraschiv, R. Royle, R. C. Mancini, and T. Johzaki, Kinetic effects and nonlinear heating in intense x-ray-laser-produced carbon plasmas, Phys. Rev. E **90**, 051102(R) (2014).

[17] S. Kato, Y. Kishimoto, and J. Koga, Convective amplification of wake field due to self-modulation of a laser pulse induced by field ionization, Phys. Plasmas **5**, 292 (1998).

[18] W. Lotz, Electron-impact ionization cross-sections for atoms up to $Z = 108$, Z. Phys. **232**, 101 (1970).

[19] A. Kramida, Yu. Ralchenko, J. Reader, and NIST ASD Team, NIST Atomic Spectra Database (ver. 5.12) (National Institute of Standards and Technology, Gaithersburg, MD, 2024), available online at https://physics.nist.gov/asd (10 July 2025).

[20] G. Ecker and W. Kröll, Lowering of the ionization energy for a plasma in thermodynamic equilibrium, Phys. Fluids **6**, 62 (1963).

[21] H.-K. Chung, M. H. Chen, W. L. Morgan, Y. Ralchenko, and R. W. Lee, FLYCHK: Generalized population kinetics and spectral model for rapid spectroscopic analysis for all elements, High Energy Density Phys. **1**, 3 (2005).

[22] M. F. Gu, The flexible atomic code, Can. J. Phys. **86**, 675 (2008).

[23] A. Bar-Shalom, M. Klapisch, and J. Oreg, HULLAC, an integrated computer package for atomic processes in plasmas, J. Quant. Spectrosc. Radiat. Transfer **71**, 169 (2001), Radiative Properties of Hot Dense Matter.

[24] R. R. Pandit, E. Ackad, E. d'Humieres, and Y. Sentoku, Ponderomotive scaling in the radiative damping regime, Phys. Plasmas **24**, 103302 (2017).

[25] A. Kon, M. Nishiuchi, Y. Fukuda, K. Kondo, K. Ogura, A. Sagisaka, Y. Miyasaka, N. P. Dover, M. Kando, A. S. Pirozhkov *et al.*, Characterization of the plasma mirror system at the J-KAREN-P facility, High Power Laser Sci. Eng. **10**, e25 (2022).